Regular nanodomain vertex arrays in BiFeO3 single crystals

Berger, A., Hesse, D., Hähnel, A., Arredondo-Arechavala, M., & Alexe, M. (2012). Regular nanodomain vertex arrays in BiFeO3 single crystals. Physical Review B (Condensed Matter), 85(6), [064104]. DOI: 10.1103/PhysRevB.85.064104

Published in:
Physical Review B (Condensed Matter)

Document Version:
Early version, also known as pre-print

Regular nanodomain vertex arrays in $BiFeO_3$ single crystals

A. Berger, D. Hesse,* A. Hähnel, M. Arredondo, and M. Alexe
Max Planck Institute of Microstructure Physics, Weinberg 2, D-06120 Halle, Germany
(Received 20 December 2011; revised manuscript received 17 January 2012; published 8 February 2012)

Domain patterns consisting of triangular nanodomains of less than 50 nm size, arranged into long regular vertex arrays separated by stripe domains, were observed by (scanning and high-resolution) transmission electron microscopy and piezoresponse force microscopy in $BiFeO_3$ single crystals grown from solution flux. Piezoresponse force microscopy analysis together with crystallographic analysis by selected area and nanobeam electron diffraction indicate that these patterns consist of ferroelectric 109° domains. A possibility for conserving Kittel's law is discussed in terms of the patterns being confined to the skin layer observed recently on $BiFeO_3$ single crystals.

DOI: 10.1103/PhysRevB.85.064104 PACS number(s): 77.80.Dj, 75.85.+t, 61.72.Nn

I. INTRODUCTION

Bismuth ferrite $BiFeO_3$ (BFO) is a unique example of an intrinsic multiferroic that simultaneously shows magnetic (antiferromagnetic), ferroelastic, and ferroelectric properties at room temperature. According to Kubel and Schmid,[1,2] BFO belongs to the group of fully ferroelectric/partly ferroelastic compounds with perovskite structure; it is ferroelectric below 1100 K and antiferromagnetic below 643 K. Due to its large polarization in thin films and the possible coupling of the latter with the magnetic moment, it has been one of the most studied ferroelectric materials during the last years.[3–6]

The room-temperature phase of BFO is rhombohedral (R3c) with a pseudocubic lattice parameter of 3.965 Å, an angle between pseudocubic ⟨100⟩ axes of about 89.4°, and with ferroelectric polarization along the [111] direction.[2] (Pseudocubic indexing is used throughout this paper; additionally, as will be discussed below, hexagonal indexes are shown in Fig. 8(d)). Despite its high paraelectric-ferroelectric transition temperature and its high distortion of the cubic unit cell at room temperature, which would suggest a high polarization, only small values of polarization of about 6 $\mu C/cm^2$ were measured in early studies on BFO single crystals.[7] Only recently, very large polarization values, of about 100 $\mu C/cm^2$ along the diagonals of the perovskite unit cell, have been measured on thin films as well as on bulk single crystals.[4,8] As mentioned, the polarization direction lies along the [111] direction, leading to the formation of eight possible polarization variants. The domain structure of BFO thin films has been studied in detail by Zavaliche *et al.*,[9] who showed three main domain types labeled upon the angle that the polarization vector forms in neighboring domains. These are two ferroelastic domains, viz. 71° and 109° domains, and one 180° pure ferroelectric domain. The ferroelastic domains of BFO may have a certain polarization discontinuity perpendicular to the domain wall, which is supposed to be the main cause for the high conductivity of these domain walls and should also play a certain role in the abnormal photovoltaic effect in BFO.[10–12] The antiferromagnetic plane is coupled with the polarization direction in such a way that the magnetic easy plane in which the spins rotate is perpendicular to the polarization vector, i.e., the [111] crystallographic direction. Ferroelastic switching in BFO also implies switching of these magnetic planes, with a significant impact on the electrical control of magnetic properties in multiferroic devices.[13]

Recently, Marti *et al.*,[14] using grazing incidence x-ray diffraction, showed that an ∼10-nm-thick surface layer of $BiFeO_3$ has an independent phase transition confined to this skin layer. They suggested that some of the anomalies of $BiFeO_3$ may also be confined to, and/or originate in, this skin layer. We have to parenthetically mention here that the surface of $BiFeO_3$, and especially the domain structure at the surface, proved to play an essential role in the exchange bias coupling between $BiFeO_3$ and adjacent magnetic layers.[15]

When judging the properties of domains and domain walls in multiferroic materials, the orientation (habit plane) of the domain wall in relation to the polarization direction has to be carefully considered.[16,17] This is the reason why we not only report on the observation of a new type of nanodomain in $BiFeO_3$ single crystals by transmission electron microscopy (TEM) and piezoresponse force microscopy (PFM), the shape and arrangement of which correspond to a linear arrangement of vertices, but also strive to analyze the geometry and orientation of the domain walls in some detail. From the observations, a reasonable domain model is derived.

II. EXPERIMENTAL METHODS

$BiFeO_3$ single crystals were grown by a method similar to that proposed by Kubel and Schmid.[1] In dependence on cooling rate, platelet-like (110)-oriented dendritic crystals or (001)-oriented rosette-like pyramidal crystals, as described by Burnett *et al.*,[18] were obtained. The (001)-oriented rosette-like pyramidal crystals were used for the present investigations. Crystal size was typically larger than 1 mm × 1 mm, with a thickness between 100 and 300 μm. For PFM investigations, the crystals were polished parallel to the (001) surface. Polishing was performed by 0.25 μm diamond paste, followed by chemical mechanical polishing (CMP) using a SiO_2 colloidal solution (Syton) diluted with water in a 1:1 ratio. TEM samples were prepared by focused ion beam (FIB) thinning, with the sample plane either parallel or perpendicular to the (001) crystal surface, and under various azimuths in the latter case. For standard and high-resolution TEM investigations, a Philips CM20T with LaB_6 cathode and a Philips CM20 with a field emission gun (FEG) were used at an acceleration voltage of

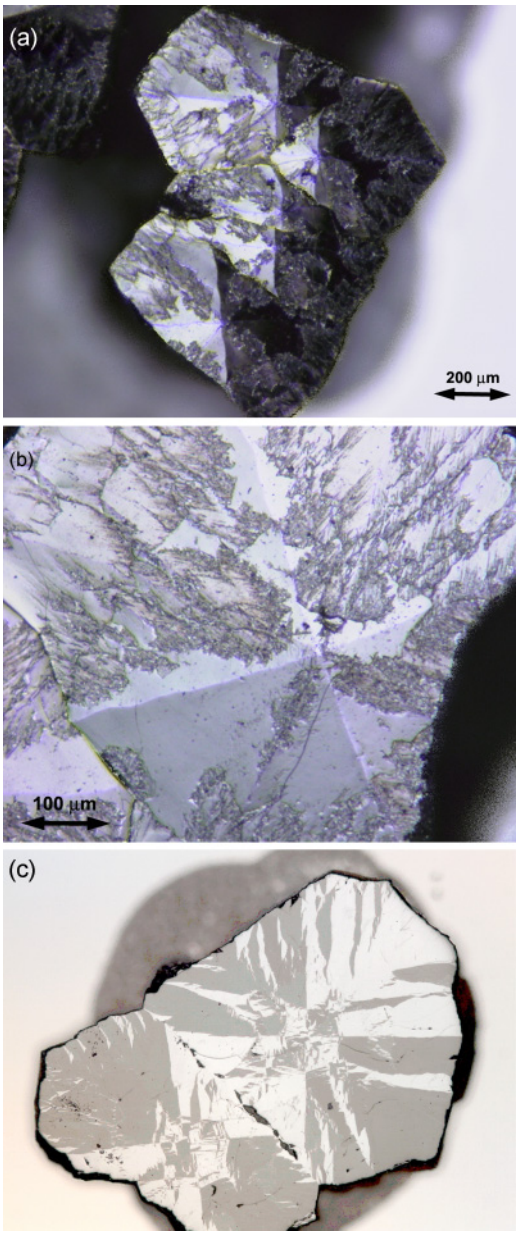

FIG. 1. (Color online) (a, b) Two optical micrographs of an as-grown $BiFeO_3$ single crystal. (c) Macroscopic ferroelastic domains revealed by polarized light on a polished (001)-oriented BFO single crystal.

200 kV, as well as a high-resolution TEM (HRTEM) Jeol 4010 at an acceleration voltage of 400 kV. Energy-dispersive x-ray (EDX) element mapping in scanning TEM (STEM) was performed in the Philips CM20 FEG, and nanobeam electron diffraction was performed in an FEI TITAN 80-300 at 300 kV with a second 20 μm condenser aperture. The aperture defines both the semiconvergence angle of 0.3 mrad and the full width at half maximum (FWHM) of the illuminating electron beam of about 3 nm in the microprobe STEM mode. Electron diffraction patterns were simulated by the JEMS program package from Pierre Stadelmann, EPFL, Lausanne, Switzerland.

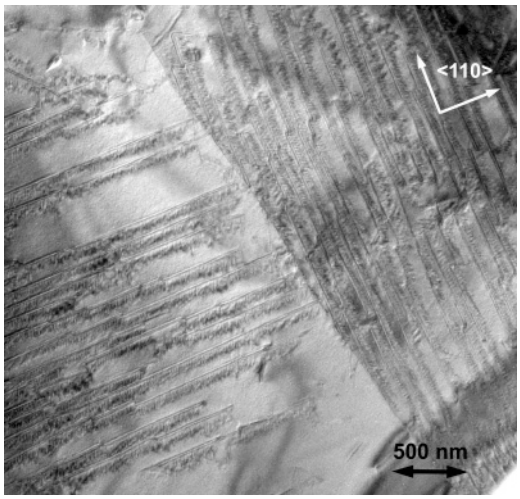

FIG. 2. TEM overview image of domain structures. Two ⟨110⟩ directions are indicated by white arrows.

III. PHENOMENOLOGY AND MORHOLOGY

Figure 1(a) and 1(b) shows two optical micrographs of as-grown BFO crystals. Within the four pyramid faces of the crystal habit, elongated patterns of surface roughness are visibly interrupting the otherwise mirror-plane surface. Macroscopic ferroelastic domains arranged apparently in a quadrant geometry are readily visible in Fig. 1(c), which is a polarized-light optical micrograph of a polished (001)-oriented BFO single crystal.

A TEM overview image taken at low magnification shows patterns of a fine ripple between long lines (Fig. 2). From this image and from a HRTEM investigation (see following), the long lines of the patterns are revealed to run along the ⟨110⟩ directions. As Fig. 2 shows, the crystal in this case contains two large regions that differ by the direction of the long lines. The latter forms an angle of about 90° left and right from the boundary between the regions. By comparing a number of samples cut perpendicular and parallel to the surface, it was found that regions of this type are present in all samples, with the long lines running in one of the possible six ⟨110⟩ directions in the volume of the crystal. The long lines are typically found to be 50 to 150 nm apart.

TEM images at higher magnification (Fig. 3) reveal that the ripple pattern consists of linear arrangements of vertices. As shown later herein in detail, it is reasonable to assume that the vertices are formed by 109° domain walls. More specifically, the domain wall pattern consists of a more or less regular array of fourfold vertices, of which two domain walls are running into a long stripe domain. The linear arrangement of the vertex array can be very regular on the 100 nm scale [Fig. 3(a)], but it can also contain defects [Fig. 3(b)], part of which resemble dislocations or grain boundaries (not shown). The overall morphology is less regular on the micron scale (Fig. 2). Qualitatively similar domain vertices were previously reported in incommensurate and α-phases of quartz, along with a corresponding analysis of the symmetry,[19] as well as in ferroelectric, rhombohedral α-GeTe single crystals (see Fig. 7 in Ref. 20).

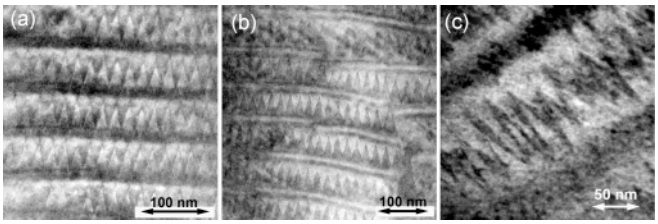

FIG. 3. Three typical TEM images of domain structures. (a,b) Sample plane perpendicular to the crystal surface, with {110} azimuth; beam direction of type ⟨110⟩. (c) Sample plane parallel to the (001) crystal surface. (a) Regular morphology; (b) morphology with defects; (c) view along ⟨100⟩ beam direction. Here, the short baseline of the triangles is further foreshortened due to the 45° tilt with respect to the ⟨110⟩ viewing directions in (a) and (b).

The individual domains have a width of about 15 to 20 nm [Figs. 3(a) and 3(b)]. The described type of patterns can be seen both in samples cut along the {100} and {110} planes. They are more clearly revealed in {110}-cut samples, at an electron beam direction close to ⟨110⟩. In a sample cut parallel to the (001) surface of the crystal, the pattern appears foreshortened in one direction, due to the sample surface being at 45° with respect to the ⟨110⟩ direction of the long lines [Fig. 3(c)]. The presence of these patterns does not affect the corresponding diffraction patterns (acquired with a selected area aperture of about 1 μm): Even in different directions, these prove to be purely single crystalline despite the presence of a large number of domain patterns with high density (Fig. 4).

The appearance of the domain pattern in TEM varies significantly, obviously due to diffraction contrast, as can be judged from dark-field images (Fig. 5) and HRTEM images (Fig. 6) acquired by varying the sample tilt. The long stripe domains are particularly visible in Figs. 3(b) and 5. EDX elemental mapping (not shown) revealed a uniform composition of the samples, not affected by the domain pattern. A nanobeam electron diffraction analysis (Fig. 7) revealed the diffraction patterns of adjacent triangular and stripe domains to be geometrically identical. However, slightly different reflection intensities were observed, pointing to subtle orientation differences between the domains.

IV. ORIENTATION OF THE DOMAIN PATTERN IN THE CRYSTAL LATTICE

Figure 8(a) shows an HRTEM image of part of a domain pattern. As can be judged from the Fourier transformation

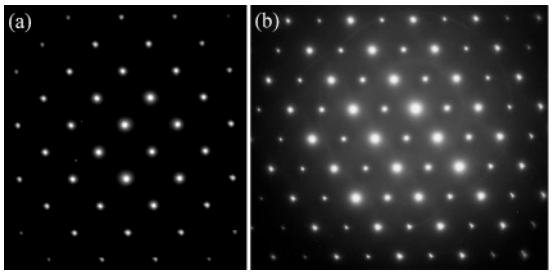

FIG. 4. Electron diffraction patterns acquired with a selected area aperture of 1 μm, containing many vertex-type nanodomain patterns of high density. Beam direction of type (a) ⟨100⟩ and (b) ⟨110⟩.

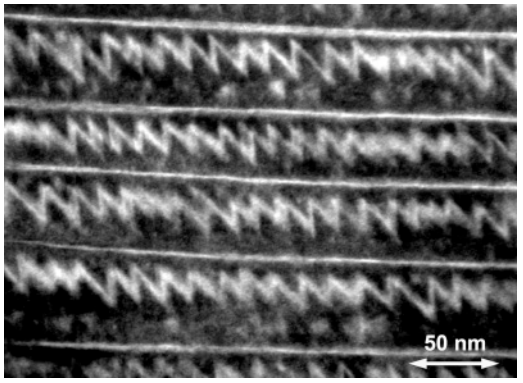

FIG. 5. Example of a TEM dark-field image.

[Fig. 8(b)] and the corresponding simulated diffraction pattern [Fig. 8(d)], the beam direction in Fig. 8 is of type ⟨110⟩. Apart from a variation of the background contrast corresponding to the triangular pattern, the different parts of the image show the same HRTEM structure image, roughly corresponding to a cubic ⟨110⟩ HRTEM image pattern. No distortions of this pattern can be recognized across the image. Colored arrows and lines in Fig. 8(c) and 8(d) show that the sharp (upper and lower) apexes of the vertex are pointing into a ⟨100⟩ direction, whereas the horizontal line (parallel to the stripe domain direction), which is perpendicular to the mentioned ⟨100⟩ direction, is along a ⟨110⟩ direction. Note that the diagonal lines correspond to two different ⟨111⟩ directions, along which the two in-plane polarization vectors are directed. For a better explanation, Fig. 9 shows a geometrical model of the vertex domains. Assuming that the A/B and A/C boundaries are plane, and also perpendicular to the paper plane, the geometrical relations shown in Fig. 9, seen from ⟨110⟩ direction, can be inferred. (Insets [a] and [b] in Fig. 9 show magnified views of the pseudocubic unit cell seen from the ⟨110⟩ direction and from slightly off the ⟨110⟩ direction, respectively.) As shown in Figs. 8(c) and 9, the A/B domain walls form angles of 71° and 109° with the ⟨111⟩ directions, leaving an angle of $(360° - 3 \times 109°) = 33°$ at the apex. In the cubic indexing of Fig. 8(d), the domain walls forming the vertices (the flanks of the 33° angle) correspond approximately to the $(\bar{2}55)$ and $(2\bar{5}5)$ planes.

In order to establish the polarization direction in each domain, piezoresponse force microscopy (PFM) was performed on polished (100)-oriented surfaces of BFO crystals (Fig. 10).

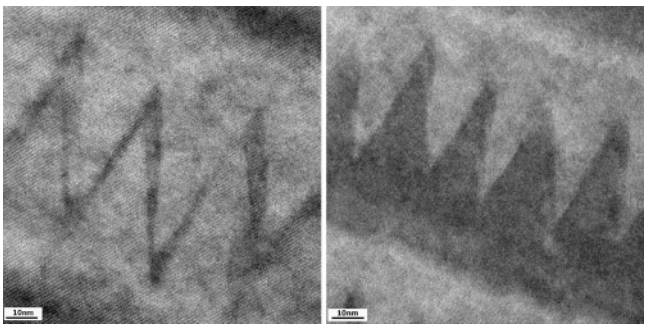

FIG. 6. Examples of HRTEM images of vertex domain structures, acquired at different sample tilts.

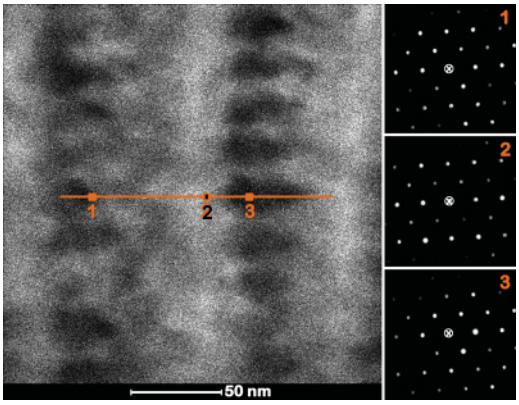

FIG. 7. (Color online) Three out of a series of nanobeam electron diffraction patterns (right) acquired with an ∼3 nm beam at the respective positions of the square moving along the horizontal line shown in the STEM image (left). In the STEM image, two linear arrays of triangular vertex domains (dark) extend vertically, with a long stripe domain (bright) in the center. (The small crossed circles mark the zero reflection.)

In particular, Fig. 10(b) and 10(e) show the complex PFM signal, viz. $A{\cdot}\cos(\theta)$, where A is the signal amplitude, and θ is the signal phase for the out-of-plane (OOP) piezoresponse [Fig. 10(b)] and for the in-plane (IP) piezoresponse [Fig. 10(e)]. In such a way, the white and dark contrasts reveal ferroelectric domains with opposite polarization, as shown by dark (blue) and gray (green) direction signs in Fig. 10(b) and corresponding dark (blue) and gray (green) arrows in Fig. 10(e). It is worth noticing that the PFM investigations show opposite contrast simultaneously in both OOP and IP images. According to Zavaliche *et al.*, this is the fingerprint of 109° or 180° domains.[9]

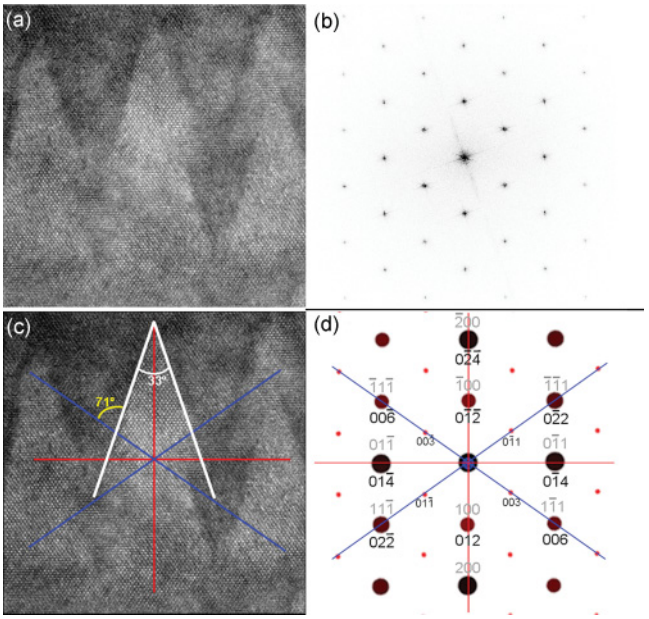

FIG. 8. (Color online) (a) HRTEM image along the beam direction ⟨110⟩ showing a number of vertex domains. (b) Fast Fourier transform of (a). (c) Same HRTEM image as (a), but with ⟨111⟩ directions (diagonal lines; blue), ⟨100⟩ direction (vertical line; red), and ⟨110⟩ direction (horizontal line; red), as well as some angles indicated. (d) Simulated hexagonal diffraction pattern along the hexagonal beam direction $[\bar{1}00]_{hex}$ (pseudocubic direction of type ⟨110⟩). The reflections are indicated by hexagonal indexes (black, below the spot) according to the hexagonal unit cell, and additionally by cubic indexes (gray, above the spot), according to the pseudocubic unit cell. The small (red) reflections are kinematically forbidden but frequently appear in electron diffraction due to dynamic effects.

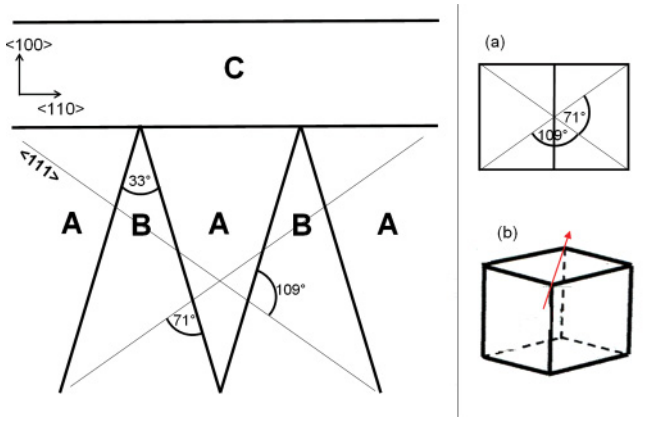

FIG. 9. (Color online) Geometric model of vertex domains, seen along a ⟨110⟩ direction, with two ⟨111⟩ directions and a number of angles indicated. Inset: Magnified unit cells seen (a) directly in the ⟨110⟩ direction, and (b) slightly off the ⟨110⟩ direction (arrow).

V. DEDUCTION OF A REASONABLE DOMAIN MODEL

From the PFM observations, it is reasonable to assume that the vertex domain pattern consists of ferroelectric nanodomains, forming a regular A-B-A-B pattern that consists

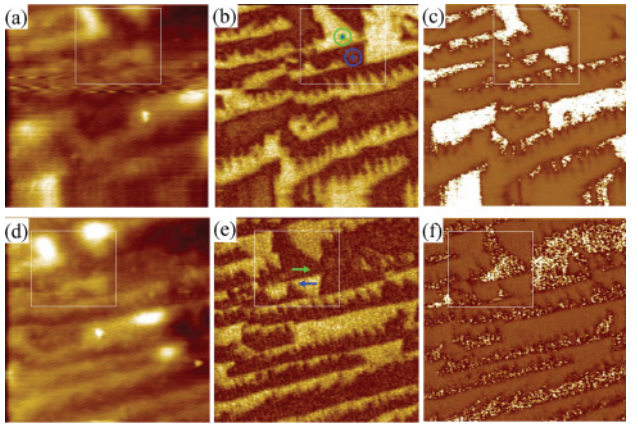

FIG. 10. (Color online) Piezoresponse force microscopy images acquired on a (100)-oriented BFO crystal. (a) and (d) are topography images; (b) and (c) are the images of complex PFM signal and phase, respectively, of the out-of-plane (OOP) piezoresponse; (e) and (f) are images of complex PFM signal and phase, respectively, of the in-plane (IP) piezoresponse. Note the slight drift toward the left that occurred between acquisition of the OOP and IP images. For convenience, the same scanned region is marked by the white square. The polarization orientation in adjacent domains is marked in (b) and (e). The size of each image is $1\mu m \times 1\mu m$.

TABLE I. The 14 models with arrangement of polarization directions in the vertex domain patterns derived from Fig. 9. Models 1 and 13 (both highlighted) are shown in Fig. 11.

Model No.	Direction of polarization in domain A	Direction of polarization in domain B	Type of A/B boundary	Approximate jump of P_S at A/B boundary ($\mu C/cm^2$)
1	In-plane up, to left	In-plane down, to left	71°	30
2	In-plane up, to left	In plane up, to right	109°	170
3	In-plane up, to left	In-plane down, to right	180°	135
4	In-plane up, to left	Out-of-plane up, to front	71°	80
5	In-plane up, to left	Out-of-plane down, to front	109°	50
6	In-plane up, to left	Out-of-plane up, to back	71°	80
7	In-plane up, to left	Out-of-plane down, to back	109°	50
8	Out-of-plane up, to front	In-plane down, to left	109°	120
9	Out-of-plane up, to front	In-plane up, to right	71°	85
10	Out-of-plane up, to front	In-plane down, to right	109°	55
11	Out-of-plane up, to front	In-plane up, to left	71°	75
12	Out-of-plane up, to front	Out-of-plane down, to front	71°	30
13	Out-of-plane up, to front	Out-of-plane up, to back	109°	zero
14	Out-of-plane up, to front	Out-of-plane down, to back	180°	30

of two different ferroelectric domains A and B, an extended ferroelectric stripe domain C, and A/B and A/C boundaries that are plane and perpendicular to the paper plane (Fig. 9). Ignoring for the moment the PFM result, the domain boundaries may be of 71°, 109°, and 180° types. Considering all possibilities of polarization directions in the domains A and B, 28 models can be derived. Additionally, one may assume that the extended large-area boundary between domains A and C is either a noncharged boundary or not a boundary at all. This is reasonable in view of the high energy related to charged boundaries, especially in a crystal of such high polarization (100 $\mu C/cm^2$ along ⟨111⟩) as BFO, from which it can be assumed that extended boundaries should be noncharged. The 28 models can be broken down to 14 models (Table I), if each pair of models that just differ by an interchange of domains A and B is combined into one model. The remaining 14 models (Table I) differ by the out-of-plane piezoresponse-related character of the A and B domains (in-plane positive or negative out-of-plane direction of the polarization in A and B), the character of the A/B boundaries (71°, 109°, or 180°), and the charge that results from the (partially) head-head or tail-tail coupling of the adjacent polarization vectors. This charge has been estimated by a geometrical approximation, drawing the perpendicular components of the polarization vector left and right from the boundary (to the A/B boundaries), measuring their length difference, dividing the difference by the length of the full ⟨111⟩-directed polarization vector, and multiplying by $|\mathbf{P_S}|$ ($|\mathbf{P_S}| = 100\ \mu C/cm^2$). The A/C boundary is a noncharged 109° boundary in most models; in the rest of the models, domains C and A are identical. Figure 11 shows two reasonable models of polarization arrangement: (i) the entire in-plane model 1 (blue polarization arrows) with 71° in-plane type A/B boundaries, and (ii) the out-of-plane model 13, i.e., the only one of the 14 models corresponding to a zero charge on the A/B domain boundaries, cf. Table I (red polarization arrows drawn inside of unit cell cubes), with 109° out-of-plane type A/B boundaries. For domain C, two variants are considered in each of the two models: The right version (right from "C") corresponds to a noncharged 109° boundary, and the left version (left from "C") corresponds to the absence of A/C domains. The latter means that there is no extended A/C boundary at all, as some of the micrographs indeed suggest (compare Figs. 6 and 8 with Fig. 11). Whereas model 1 does not fit the PFM observations, model 13 fully corresponds to the PFM observations (cf. Fig. 10), because the direction of the ferroelectric polarization is out-of-plane, and it changes from "into the sample" to "out of the sample" crossing the A/B boundaries, and because all the involved domain boundaries are 109° boundaries. Model 14, involving 180° A/B boundaries, is considered to be less probable compared to model 13, due to a nonzero charge of the former.

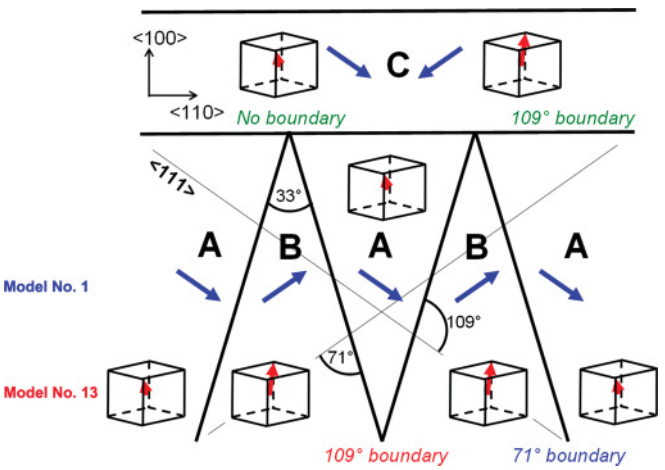

FIG. 11. (Color) Two models of polarization arrangement: The entire in-plane model 1 (blue polarization arrows) with 71° in-plane type A/B boundaries, and model 13, i.e., one of the 14 models corresponding to the least value of charge on A/B domain boundaries (red polarization arrows in unit cell cubes) with 109° out-of-plane type A/B boundaries. For domain C, two variants are considered in each of the two models: The left version (left from "C") corresponds to an absence of A/C domains, and the right version (right from "C") corresponds to a noncharged 109° boundary. (Crystallographic details as in Fig. 9.)

The slight intensity variations observed within the otherwise stable nanodiffraction pattern, when crossing the domain boundaries (Fig. 7), indicate a small orientation deviation among A, B, and C domains, most probably due to the rhombohedral distortion of the unit cell; for simplicity, the structure had been considered cubic in the models of Figs. 9 and 11. For example, within the cubic approximation, the beam direction of both A and B domains is ⟨110⟩, whereas in reality, the rhombohedral distortion will result in a slight deviation between the beam directions of A and B domains. Since the rhombohedral distortion is considerably large[2] and in model 1 extends laterally along the polarization direction (blue arrows in Fig. 11), model 1 would result in quite an extensive distortion of the diffraction pattern switching the nanobeam from A to B, whereas in model 13, the corresponding visible distortions are small, which additionally supports this model. The absence of spot splitting in Fig. 4 also speaks in favor of an out-of-plane model like model 13.

VI. DISCUSSION AND CONCLUSIONS

The impact of ferroelectric domains on the properties of ferroelectric materials cannot be overestimated. The observed arrays of nanodomain vertexes of high density in $BiFeO_3$ single crystals should therefore be of interest. The present paper does not present a full characterization of the observed nanodomain arrays. Rather, it strives to summarize the observed findings and to bring them into a reasonable relation. The joint observation of TEM and PFM contrasts, and their interpretation, clearly points to the presence of arrays of ferroelectric and ferroelastic 109° nanodomain vertexes in BFO single crystals that have hitherto not been described.

Ferroelectric domains of triangular shape, with a base length between 15 and 30 nm, and a height of about 25 to 50 nm, form the geometrical repetition unit of these arrays. The domain boundaries (flanks of the triangles) form characteristic angles of 71° and 109° with the in-plane ⟨111⟩ directions in the sample, and the apex of the triangle includes an angle of 33°. The triangles form chains along the ⟨110⟩ directions; two chains are separated by a stripe domain extending along the same direction. A reasonable geometric-crystallographic model has been derived under plausible assumptions. In this model, all observed domain boundaries are ferroelectric 109° boundaries, and the polarization vectors in the various domains point out of the sample plane, viz. into the depth of the sample in one domain, and out of the sample in the neighboring domain. This corresponds well to the observed contrast in the vertical PFM images. Further investigations are required to shed more light on these nanodomains. However, considering the possible role of domain boundaries and their orientations for the anomalous photovoltaic effect in BFO,[11] the significance of the observation of these arrays of ferroelectric/ferroelastic nanodomains in BFO single crystals cannot be overestimated. In principle, a common origin of the observed vertex domains and topological defects induced in BFO[21] (observed in other multiferroic materials as well[22]) may also be suggested.

We should note that this fine domain pattern would be in conflict with the rather general statement of the Kittel law, which asserts that the domain size should scale with the square root of the crystal thickness or, more generally, with the correlation length of the system.[23,24] Thus, we should not exclude the possibility that these domains are confined only to the skin layer (of 10 nm thickness or less) of $BiFeO_3$ single crystals, which was recently found by Marti *et al.*[14] This would reconcile the fine domains revealed by the present PFM and TEM investigations—both methods in this case would detect only the skin layer of the bulk and thinned samples, respectively—and the macroscopic domains detected by polarization optical investigations [Fig. 1(b)].

At the end, we may speculate on the influence of these dense arrays of ferroelastic domains on the bulk properties of BFO. If these domains are uniformly distributed throughout the entire bulk of the BFO crystal, the ferroelectric switching would be hampered to a very large extent. This might explain the difference between the large values of polarization close to theoretical values measured recently on single-domain single crystals[8] and the small values measured in the early work.[7] On the other side, a similar argument might explain the small value of the polarization that still exists in ceramic materials compared to single crystals: The polycrystalline nature of ceramics involves a much larger surface-to-bulk ratio than a single crystal, and, if the observed kind of domain pattern is confined to the skin of the crystal, again the switching would be hampered. Finally, we may also speculate on a correlation between the particular photocatalytic properties of BFO[25] and the existence of such a particular form of the domain pattern at the crystal surface.

ACKNOWLEDGMENTS

The authors are thankful to Gustau Catalan for useful discussions and suggestions regarding the skin layer, Norbert Schammelt for the FIB preparations, and Florian Johann for a careful reading of the manuscript and for valuable discussions. This work has been supported by German Research Foundation (DFG) via Coordinated Research Project SFB 762.

*hesse@mpi-halle.de

[1] F. Kubel and H. Schmid, J. Cryst. Growth **129**, 515 (1993).
[2] F. Kubel and H. Schmid, Acta Crystallogr. B **46**, 698 (1990).
[3] G. Catalan and J. F. Scott, Adv. Mater. **21**, 2463 (2009).
[4] J. Wang, J. B. Neaton, H. Zheng, V. Nagarajan, S. B. Ogale, B. Liu, D. Viehland, V. Vaithyanathan, D. G. Schlom, U. V. Waghmare, N. A. Spaldin, K. M. Rabe, M. Wuttig, and R. Ramesh, Science **299**, 1719 (2003).
[5] M. P. Cruz, Y. H. Chu, J. X. Zhang, P. L. Yang, F. Zavaliche, Q. He, P. Shafer, L. Q. Chen, and R. Ramesh, Phys. Rev. Lett. **99**, 217601 (2007).
[6] T. Zhao, A. Scholl, F. Zavaliche, K. Lee, M. Barry, A. Doran, M. P. Cruz, Y. H. Chu, C. Ederer, N. A. Spaldin, R. R. Das, D. M. Kim, S. H. Baek, C. B. Eom, and R. Ramesh, Nat. Mater. **5**, 823 (2006).
[7] J. R. Teague, R. Gerson, and W. J. James, Solid State Commun. **8**, 1073 (1970).

[8]D. Lebeugle, D. Colson, A. Forget, and M. Viret, Appl. Phys. Lett. **91**, 022907 (2007).
[9]F. Zavaliche, S. Y. Yang, T. Zhao, Y. H. Chu, M. P. Cruz, C.B. Eom, and R. Ramesh, Phase Trans. **79**, 991 (2006).
[10]J. Seidel, L. W. Martin, Q. He, Q. Zhan, Y. H. Chu, A. Rother, M. E. Hawkridge, P. Maksymovych, P. Yu, M. Gajek, N. Balke, S. V. Kalinin, S. Gemming, F. Wang, G. Catalan, J. F. Scott, N. A. Spaldin, J. Orenstein, and R. Ramesh, Nat. Mater. **8**, 229 (2009).
[11]S. Y. Yang, J. Seidel, S. J. Byrnes, P. Shafer, C. H. Yang, M. D. Rossell, P. Yu, Y. H. Chu, J. F. Scott, J. W. Ager, L. W. Martin, and R. Ramesh, Nature Nanotech. **5**, 143 (2010).
[12]P. Maksymovich, J. Seidel, Y. H. Chu, P. Wu, A. P. Baddorf, L.-Q. Chen, S. V. Kalinin, and R. Ramesh, Nano Lett. **11**, 1906 (2011).
[13]S. M. Wu, S.A. Cybart, P. Yu, M. D. Rossell, J. X. Zhang, R. Ramesh, and R. C. Dynes, Nat. Mater. **9**, 756 (2010).
[14]X. Martí, P. Ferrer, J. Herrero-Albillos, J. Narvaez, V. Holy, N. Barrett, M. Alexe, and G. Catalan, Phys. Rev. Lett. **106**, 236101 (2011).
[15]Y.-H. Chu, L. W. Martin, M. B. Holcomb, M. Gajek, S.-J. Han, Q. He, N. Balke, C.-H. Yang, D. Lee, W. Hu, Q. Zhan, P.-L. Yang, A. Fraile-Rodríguez, A. Scholl, S. X. Wang, and R. Ramesh, Nat. Mater. **7**, 478 (2008)
[16]E. A. Eliseev, A. N. Morozovska, G. S. Svechnikov, V. Gopalan, and V. Ya. Shur, Phys. Rev. B **83**, 235313 (2011).
[17]D. Meier, J. Seidel, A. Cano, K. Delaney, Y. Kumagai, M. Mostovoy, N. A. Spaldin, R. Ramesh, and M. Fiebig, Preprint e-print arXiv:1112.5194 (2011).
[18]T. L. Burnett, T. P. Comyn, and A. J. Bell, J. Cryst. Growth **285**, 156 (2005).
[19]P. Saint-Gregoire, V. Janovec, E. Snoeck, C. Roucau, and Z. Zikmund, Ferroelectrics **125**, 209 (1992).
[20]M. Snykers, P. Delavignette, and S. Amelinckx, Mater. Res. Bull. **7**, 831 (1972).
[21]R. K. Vasudevan, Y.-C. Chen, H.-H. Tai, N. Balke, P. Wu, S. Bhattacharya, L. Q. Chen, Y.-H. Chu, I. N. Lin, S. V. Kalinin, and V. Nagarajan, ACS Nano **5**, 879 (2011).
[22]M. Safrankova, J. Fousek, and S. A. Kizaev, Czech. J. Phys. **17**, 559 (1967).
[23]C. Kittel, Phys. Rev. **70**, 965 (1946).
[24]J. F. Scott, J. Phys. Condens. Matter **18**, R361 (2006).
[25]F. Gao, X. Y. Chen, K. B. Yin, S. Dong, Z. F. Ren, F. Yuan, T. Yu, Z. Zou, and J. M. Liu, Adv. Mater. **19**, 2889 (2007).